Limits to Strong Coupling of Excitons in Multilayer WS$_2$ with Collective Plasmonic Resonances

Shaojun Wang,[†*] **Quynh Le-Van,**[†] **Fabio Vaianella,**[#] **Bjorn Maes,**[#] **Simone Eizagirre Barker,**[†]

Rasmus H. Godiksen,[‡] **Alberto G. Curto,**[‡] **and Jaime Gomez Rivas**[†,‡*]

[†] Dutch Institute for Fundamental Energy Research, Eindhoven, The Netherlands

[#] Micro- and Nanophotonic Materials Group, Faculty of Science, University of Mons, 20 place du Parc, B-7000 Mons, Belgium

[‡] Department of Applied Physics and Institute for Photonic Integration, Eindhoven University of Technology, Eindhoven, The Netherlands

ABSTRACT: We demonstrate the strong coupling of direct transition excitons in tungsten disulfide (WS$_2$) with collective plasmonic resonances at room temperature. We use open plasmonic cavities formed by periodic arrays of metallic nanoparticles. We show clear anti-crossings with monolayer, bilayer and thicker multilayer WS$_2$ on top of the nanoparticle array. The Rabi energy of such hybrid system varies from 50 to 100 meV from monolayer to sixteen layers, while it does not scale with the square root of the number of layers as expected for collective strong coupling. We prove that out-of-plane coupling components can be disregarded since the normal field is screened due to the high refractive index contrast of the dielectric layers. Even though the in-plane dipole moments of the excitons decrease beyond monolayers, the strong in-plane field distributed in the flake can still enhance the coupling strength with multilayers. The achieved coherent coupling of TMD multilayers with open cavities could be exploited for manipulating the dynamics and transport of excitons in 2D semiconductors and developing ultrafast valley/spintronic devices.

1

KEYWORDS: *light-matter interaction, exciton-polaritons, plasmonics, surface lattice resonances, 2D semiconductors, transition metal dichalcogenides.*
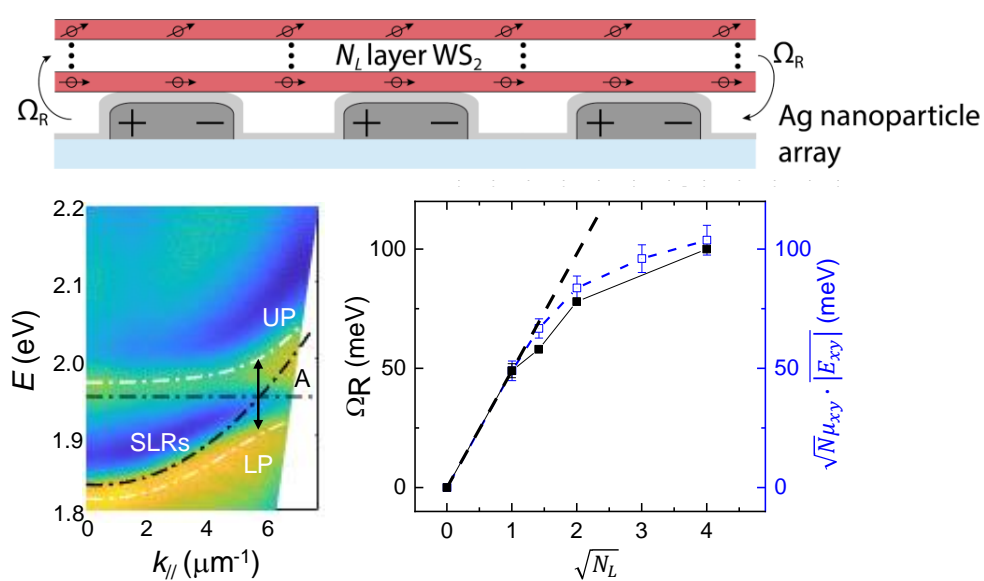
TOC Graphic

Atomically-thin transition metal dichalcogenides (TMDs, with chemical formula MX_2, M = Mo, W; X = S, Se, Te) are being intensively studied in the context of light-matter interaction after the indirect to direct band gap crossover in monolayers was established.[1–6] The remarkable optical response in such two-dimensional (2D) semiconductors originates from the strongly allowed excitonic resonances, displaying a large absorption coefficient in the visible and near-infrared.[1,7] The optically generated electron-hole pairs (excitons) in such 2D systems have exceptionally large binding energies (> 0.3 eV),[8] small Bohr radii (~ 1 nm),[9] and a new valley degree of freedom arising from the strong spin-orbit coupling and the absence of inversion symmetry of the monolayers.[10,11] These promising optoelectronic properties of excitons in 2D-TMDs provide an elegant platform to investigate strong light-matter interaction[12–16] as well as open possibilities for novel device architectures.

The regime of strong coupling between light and excitons in semiconductors to form exciton-polaritons is reached when the energy exchange between the excitonic transitions and a resonant optical mode is faster than their decoherence rates.[17,18] The spectral signature of strong coupling is the splitting of the absorption band of excitons into two new bands, corresponding to the upper and lower polaritonic states. The energy splitting of these states at resonance measures the coupling strength (*i.e.*, the Rabi energy, Ω_R) and it depends on the electromagnetic field per photon E of the optical mode, the transition dipole moment μ of the exciton and $\sqrt{N}$, where N is the number of excitons within the volume of the optical mode (*i.e.*, $\Omega_R = 2\sqrt{N}E\cdot\mu$).[17–19] Excitons in TMD monolayers with a large transition dipole moment have been demonstrated to couple strongly with different optical resonators, such as microcavities,[12,13,15,20] photonic crystals,[21] and plasmonic systems.[14,15,22–25] The hybridization of excitons in TMD monolayers with optical resonators plays an important role in fascinating phenomena, such as valley-selective chiral coupling,[22] thermally or electrically tuneable composition of the hybrid states,[23,26] and enhanced nonlinear optical susceptibility.[25] So far, most research has focused on

the strong coupling of bright excitons in monolayers due to their well-known direct optical band gap and in-plane dipole moment.[12-15,20-27] For multilayer TMDs, the orientation of the excitonic dipole moments is still an open question and the energetically indirect transitions shown in their emission spectra are reminiscent of the ultrafast decoherence rate of direct transition excitons. Only two publications have recently reported strong coupling in different thickness of multilayer TMDs to plasmonic modes.[16,27] In both publications the coupling to single metallic nanoparticles has been investigated, where the mode volume is in the nanometric scale and delocalized properties arising from the strong coupling, such as enhanced exciton-polariton transport[28,29] and long distance energy transfer,[30,31] cannot be achieved. Strong coupling of multilayer TMDs to extended plasmonic cavities is still an unexploited territory.

In this Letter, we demonstrate the strong coupling of excitons in WS_2 from monolayers to sixteen layers with optical modes in extended open plasmonic cavities formed by periodic arrays of metallic nanoparticles. The nanoparticles support localized surface plasmon resonances (LSPRs), i.e., coherent oscillations of the free electrons in the nanoparticle driven by the electromagnetic field. LSPRs are interesting for optical control of excitons in close proximity of the nanoparticles because their small electromagnetic mode volume can lead to high coupling efficiencies.[16,27,32,33] However, inherent to this small mode volume is also high losses.[32,34] Interestingly, periodic arrays of metallic nanoparticles support surface lattice resonances (SLRs), which are collective plasmonic resonances arising from the enhanced radiative coupling of LSPRs through diffracted orders in the plane of the array, also known as Rayleigh anomalies (RAs).[35–39] The quality factor of SLRs, which is inversely proportional to the loss, can be orders of magnitude larger than that of LSPRs.[35,36,39–42] Consequently, from the dynamic point of view, SLRs increase the cycles of Rabi oscillations in the strongly coupled system before dephasing.[43] In addition, the dispersive behavior of SLRs, mainly defined by the periodicity of the array and the polarizability of the constituent nanoparticles, provides an easy

4

mechanism to observe the evidence of strong coupling, i.e., anti-crossing of lower and upper
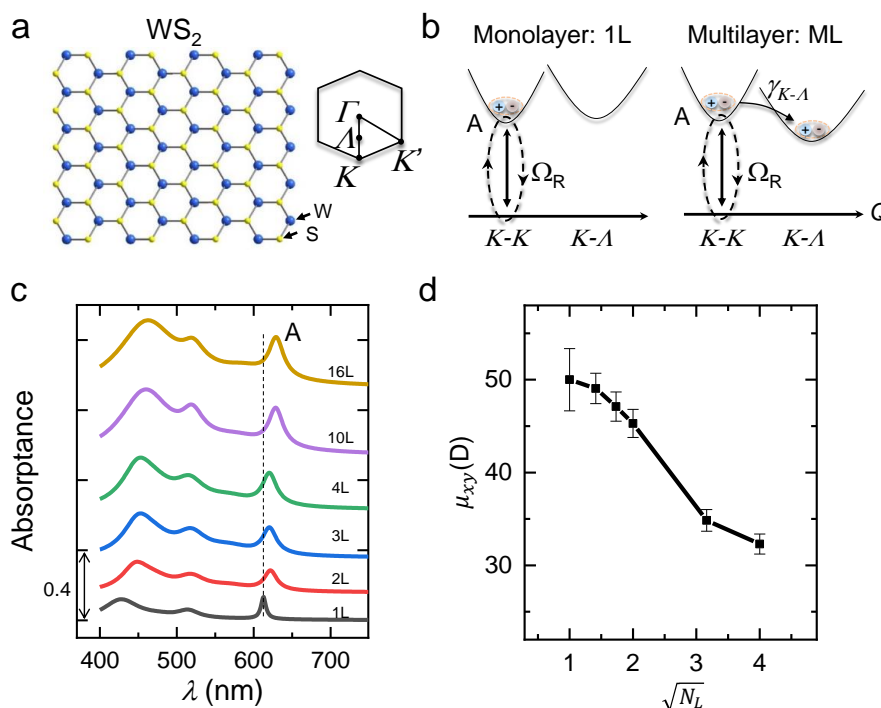
polariton bands.[34]

Figure 1. *Absorption spectra and energy diagram of WS₂.* (a) Crystal structure (top view) of WS_2 and its associated Brillouin zone. The blue and yellow circles represent the element W and S, respectively. (b) Schematic energy diagram of direct excitonic transitions (*K-K* or *K'-K'*) in WS_2 monolayer and multilayer, strongly coupled to an optical resonator as represented by the Rabi oscillation Ω_R. For the multilayer, the excitons generated at the *K / K'* points of the Brillouin zone are thermally scattered into the energetically lower Λ valleys (*K- Λ*). Q represents the center of mass momentum of the exciton. (c) Absorption spectra of a monolayer (1L, black line), bilayer (2L, red), trilayer (3L, blue), four-layer (4L, green), ten-layer (10L, maroon), and sixteen-layer (16L, orange) of WS_2 on polydimethylsiloxane (PDMS) substrates, calculated by fitting the experimental transmittance spectra using a multi-Lorentzian model and the transfer matrix method. The peaks at lowest energy correspond to A-exciton transitions in WS_2. (d) In-plane dipole moments of the A excitons of WS_2 as a function of the square root of the number of WS_2 layers, $\sqrt{N_L}$.

We used atomically thin layers of WS_2 (Figure 1a) to reach the strong coupling regime due

to the sharp and intense absorption peak of their A excitons.[15,20] To characterize the in-plane

excitonic dipole moments, we have measured the normal incidence transmittance spectra

through two WS_2 flakes with a monolayer (abbreviated to 1L) and a multilayer (ML) formed

by 10 layers (10L) and 16 layers (16L) on sample I (Figures S2a and c) and another 1L, bilayer

(2L), trilayer (3L), and four-layer (4L) on sample II (Figure 2c). The in-plane refractive index

5

(Figures S4c,d) and the normal incidence absorptance spectra (Figure 1c) of each region were calculated by fitting the transmittance spectra using a multi-Lorentzian model and the transfer matrix method (TMM) (Figures S4a and b).[15,44] As can be appreciated in Figure 1c and Figure S5a, the absorption peak around 613 nm of A excitons in the 1L is redshifted by 9 nm in 2L, 3L and 4L measured on the same flake. When the thickness of the flake is increased to 16L, the A exciton resonance is further shifted towards 629 nm, approaching the bulk value. In addition, the absorptance per layer at the A excitonic transition (Figure S5b) decreases by increasing the number of layers. The linewidth (γ_A) of the ML is nearly constant at ~ 60 meV and broader than the linewidth of 1L ~ 25 meV. To evaluate the in-plane dipole moment μ_{xy}, the absorptance per layer (abs) is spectrally integrated for the A excitonic transition (Figure S5a). We have determined the evolution of μ_{xy} as a function of the number of layers based on the relationship $\mu_{xy} \propto \sqrt{abs}$ and using the value for 1L of μ_{xy} ~ 50 Debye (D) obtained from the literatures.[33,45] The results (Figure 1d) reveal that the in-plane dipole moments gradually decrease to ~ 30 D for 16L, which we attribute to the dielectric screening and the increase of out-of-plane dipole moments when the interlayer coupling delocalizes excitons between planes.[16] Understanding the excitonic dipole components in WS_2 will help us to elucidate the nature of the coupling with the electric field of the SLRs as addressed below.

The absorption peak of A excitons in the 1L and ML is known to arise from direct band gap transitions at the K and K' points of the associated first Brillouin zone (Figure 1a, inset).[1,2] From the photoluminescence (PL) spectra (Figure S3d), excitons generated at the K / K' in the ML are mostly thermally scattered into the energetically lower Λ valleys (K-Λ).[46] The increased decoherence paths in ML homogeneously broaden the linewidth of A excitonic transitions in PL spectra. The energy diagrams in the exciton picture are shown in Figure 1b for the case of the 1L and the ML. Both 1L and ML can strongly couple with a resonant optical mode when their direct transitions exchange energy with this mode at a Rabi rate (Ω_R) faster than the

intravalley decoherence rate (γ_{K-K}) or intervalley scattering rate ($\gamma_{K-\Lambda}$) of the A excitons (i.e.,

$\Omega_R > \gamma_{K-K}, \gamma_{K-\Lambda}$). A similar strong coupling mechanism has been proved in a push-pull molecular

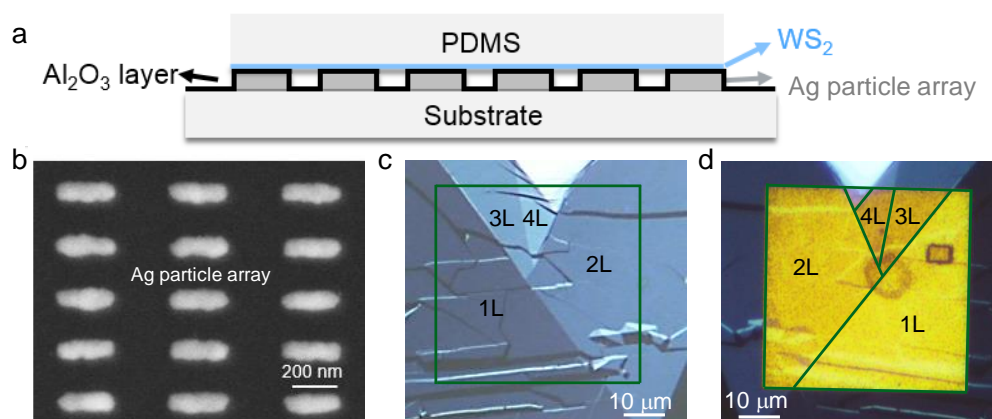system with large Stoke shift emission.[47]

Figure 2. *Sample images.* (a) Schematic side view of the sample. WS$_2$ on superstrate of PDMS is spatially separated from the particle array by a conformal alumina layer. (b) Scanning electron microscope image (top view) of the particle array. (c)(d) Optical micrograph (top view) of a WS$_2$ flake with 1L, 2L, 3L and 4L regions before and after transfer onto the particle array (square of side 50 μm).

We have coupled the 2D-semiconductor to SLRs confined on plasmonic lattices, as the one

shown in the scanning electron microscope image of Figure 2b. The plasmonic lattice consists

of an array of silver (Ag) nanoparticles with a horizontal lattice constant $P_x = 420$ nm and a

vertical lattice constant $P_y = 200$ nm. The individual nanoparticles are nanorods with a height

of 35 nm, a length of 230 nm, and a width of 70 nm. We have chosen a rectangular shape for

the nanoparticles to increase their polarizability. This polarizability is proportional to the

particle volume and it can be increased by making the particles longer while keeping the width

constant to avoid shifting the resonance frequency for a polarization along the width. Increasing

the polarizability of the nanoparticles enhances the extinction and facilitates the excitation of

SLRs. The array, with a size of 50×50 μm^2, was fabricated on a fused silica substrate by

electron-beam lithography. Each nanoparticle is coated with a 3-nm-thick atomic-layer-

deposited Al$_2$O$_3$ film that protects it from degradation and also prevents charge transfer between

the semiconductor and silver. The investigated sample consists of a mechanically exfoliated

WS$_2$ flake covering a plasmonic nanoparticle array (Figure 2d). To ensure high-quality samples, we exfoliated flakes on a flexible polydimethylsiloxane (PDMS) substrate (with a thickness of 100 μm) and we softly transferred them onto a particle array. The PDMS substrate was left as a dielectric superstrate coating for the particle array (see details in **Methods**). The final sample geometry is shown in Figure 2a. The regions with 1L, 2L, 3L, and 4L of WS$_2$ on the array are marked in Figure 2d by the green curves. They show a significant change in color depending on whether the flake is on the fused silica substrate or on the particle array. The color change indicates that the optical resonances supported by the nanoparticle array can significantly modify the reflectivity of the atomically thin material. We should note that the color change on the particle array is not simply due to the thin air spacer between the substrate and the PDMS, since the flake still shows a similar color change after the superstrate of PDMS on top is peeled off (Figure S2c).

In order to obtain the dispersion of the coupled system, we have recorded angle-resolved white-light reflection spectra of sample II with a Fourier spectroscopy microscope.[15] The orientation of the plasmonic lattice is fixed by aligning its long axis vertical to the slit of the spectrometer. The direction of a polarizer parallel or perpendicular to the slit defines the *p*-(TM) or *s*-(TE) polarization of the reflected light, respectively. The angular dispersion of SLRs along the (0, ±1) RAs of the bare particle array measured with *p*-polarized light is shown in Figure 3a. We plot the evolution of the spectra with varying angle of incidence $\theta = 0^\circ$ to 35° in Figure 3f. The angular dispersion of SLRs has a parabolic shape (Figures 3a and S7a) and results from the radiative coupling between the LSPRs of the individual particles at 525 nm (2.36 eV), enhanced by the in-plane diffraction of the RAs. We have extracted the linewidths of the SLRs by fitting the reflection spectra to a Fano-like line shape.[48] The spectral full width at half maximum (FWHM) of SLRs, Γ_{SLRs}, also has a dispersive behavior (Figure S7d), increasing

from 43 meV at $\theta = 0^o$ to 73 meV at $\theta = 35^o$ as the weight fraction of LSPRs increases in the
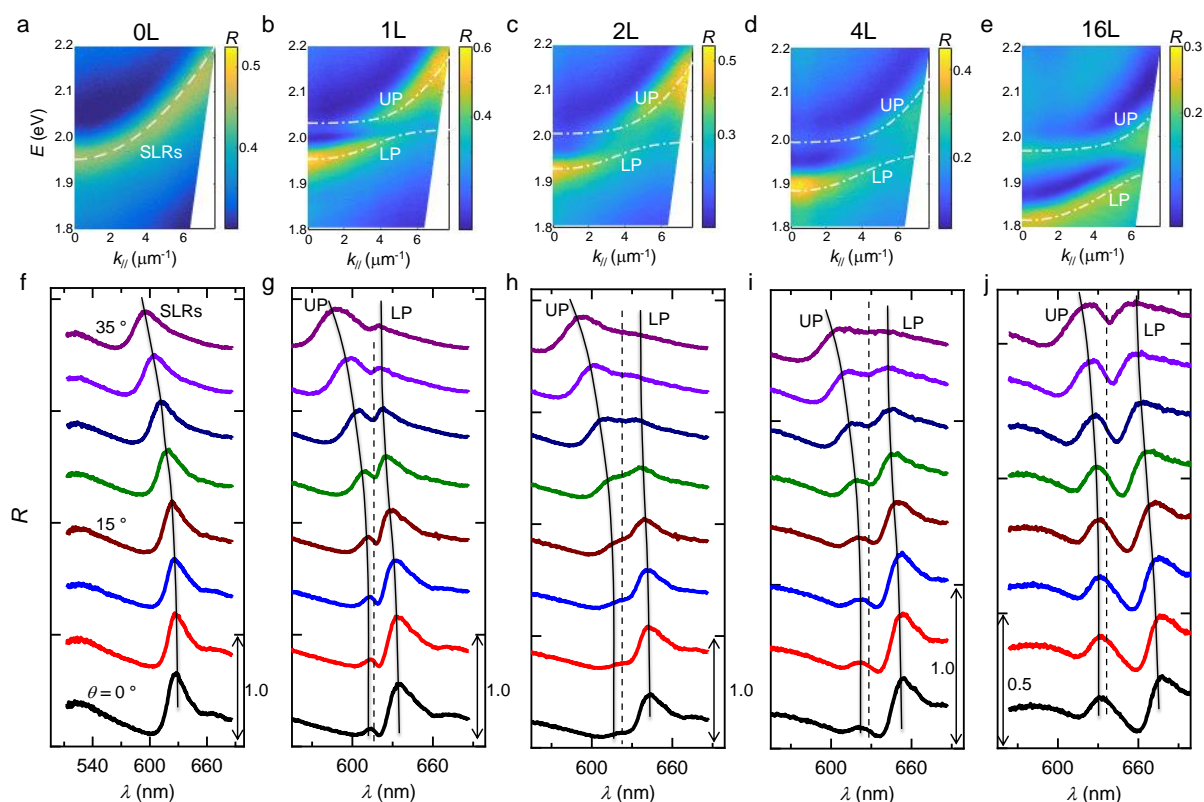
hybrid SLRs.

Figure 3. *Dispersion measurements*. (a) Angle-resolved reflection spectra of the bare nanoparticle array (0L), (b) 1L, (c) 2L, (d) 4L, and (e) 16L WS_2 on top of the array. The spectra are analyzed in *p*-(TM) polarization. The angular dispersion of each sample is fitted with the two coupled oscillator model. The dashed white curves in (a) describe the dispersion of the surface lattice resonances (SLRs) of the bare particle array. The dashed-dotted white curves in (b-e) show the dispersion of the upper polariton (UP) band and the lower polariton (LP) band. (f-j) Reflection spectra as a function of the angle of incidence from $\theta = 0°$ to 35° obtained by cutting through the corresponding Fourier images in (a-e). The solid curves in (f-j) represent the SLRs and polariton bands. The vertical dashed lines in (g-j) represent the A excitonic energy in WS_2 obtained from the reflection peaks of the bare flakes shown in Figs. S4e and S6.

On the part of the monolayer transferred on top of the array, the parabolic dispersion curves

split into two new bands corresponding to the upper (UP) and lower polariton (LP) bands

(Figure 3b). This unambiguous anti-crossing is also seen in the angular evolution of spectra

shown in Figure 3g. The hybrid system can be approximately described with a two coupled

harmonic oscillator model:[38,39,49]

$$\begin{bmatrix} \omega_{SLRs} - i\frac{\Gamma_{SLRs}}{2} & g \\ g & \omega_A - i\frac{\gamma_A}{2} \end{bmatrix} \begin{pmatrix} \alpha \\ \beta \end{pmatrix} = \omega \begin{pmatrix} \alpha \\ \beta \end{pmatrix}, \qquad (1)$$

where ω_{SLRs} and ω_A are the energies of the bare SLRs and A excitons respectively, γ_A represents the linewidth of excitons by considering the linewidth as the decoherence rate of excitons due to homogeneous broadening, and g is the coherent coupling strength. Diagonalizing the Hamitonian matrix yields new polaritonic eigenvalues $\omega_\pm$, defining the energies of UP and LP bands, and the Hopfield coefficients α and β,[50] the square of which defines the weight fractions of excitons and SLRs with $|\alpha|^2 + |\beta|^2 = 1$. The value of Rabi-splitting, $\omega_+ - \omega_- = \sqrt{4g^2 - \frac{(\Gamma_{SLRs} - \gamma_A)^2}{4}}$, is given at the condition of zero detuning, namely, $\omega_{SLRs} - \omega_A = 0$. By fitting the peak positions of the UP and LP bands in Figures 3b and g to the model, we have extracted ω_{SLRs} and the weight fractions assuming $\omega_A = 2.023$ eV, which was determined from the reflection peak of A exciton. The hybrid bands and the weight fractions of the LP are shown in Figures S8a and d, respectively. The Rabi energy, $\Omega_R = 2g = 52$ meV, is given at the in-plane wave vector $k_{//} = 4.3$ μm^{-1} when the UP or LP state is half mixed with SLRs and half with excitons, $i.e.$, $|\alpha|^2 = |\beta|^2 = \frac{1}{2}$. This analysis indicates that the spectra of uncoupled SLRs redshift 4 nm (Figures S7a and S8a) when the 1L WS$_2$ is transferred on top of the particle array. Using the same method, we have characterized the angular dispersion and coupling parameters in all the regions of interest on Samples I and II. The reflection spectra of 2L, 4L on sample II, and 16L on the particle array of sample I are plotted in Figures 3h, i, and j, respectively. As illustrated in these figures with the solid curves, the LP and UP bands are obtained by fitting the peaks for the 1L, 2L, 4L and 16L as shown in Figure S8a-c and S7c.
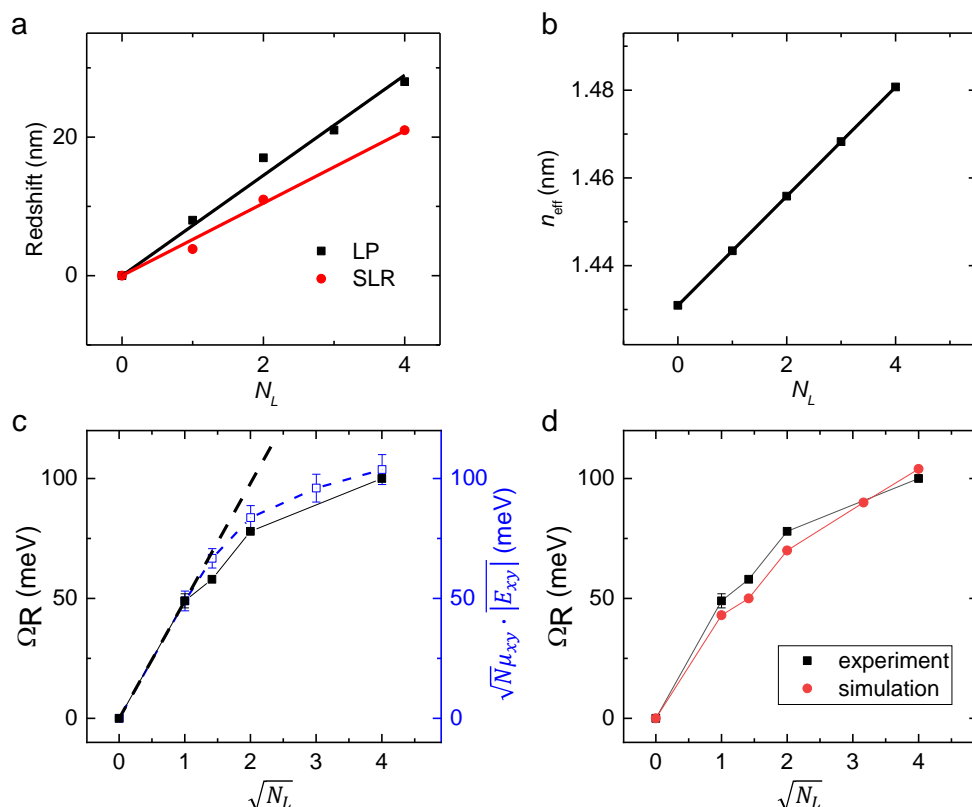
Figure 4. *Interaction between SLRs and WS₂.* (a) Linear redshift of the LP band (black squares) and the SLRs (red dots) as a function of the number of layers (N_L from 0L to 4L) of WS$_2$. The peak wavelengths of LP band are obtained from the consistent reflection and transmission spectra (Fig. S10) measured at normal incidence. The resonant wavelengths of bare SLRs are extracted from fitting the angular dispersion of the coupled system (Fig. S9). (b) Effective refractive index of the particle array as a function of N_L calculated from the grating equation and the linear slope of bare SLRs shown in (a). (c) Measured (black circles) and estimated (blue triangles) Rabi energy Ω_R as a function of the square root of N_L. The estimation is based on the formula of vacuum coupling strength $g = \sqrt{N}\boldsymbol{E}\cdot\boldsymbol{\mu}$, and herein we only account for the in-plane coupling due to the screened normal field. The dashed black line represents the linear relationship between Ω_R and $\sqrt{N_L}$ when the dot product of $\boldsymbol{\mu}$ and $\boldsymbol{E}$ is constant. The errors of the estimated Rabi-energies are due to the errors in the determination of the dipole moments (Fig. 1d) and the in-plane field amplitudes (Fig. 5f). (d) Comparison of the measured (black) and simulated (red) Rabi-energy Ω_R, obtained from reflection calculations as a function of the angle of incidence (full data shown in Fig. S12), as a function of $\sqrt{N_L}$.

The energy splitting revealed by the two solid lines in Figures 3g-j becomes larger at the resonant condition when increasing the thickness of the flake. In addition, the LP band at normal incidence redshifts linearly as a function of number of layers (Figure 4a) when comparing the reflection and extinction spectra of 0L to 4L (Figure S9) on the particle array. In order to extract the bare SLRs, we fitted the angular dispersions of different regions with the coupled oscillator

model (Figures S7 and S8) and found that the bare SLRs also varies linearly (Figure 4a) from

0L to 4L. From the grating equation (see **Methods**), the resonant wavelength of (0, ±1) RAs

can be calculated by $\lambda_{RAs} = n_{eff} \cdot P_x$, where n_{eff} is the effective refractive index defining the phase

velocity of the RAs. In the case of the bare particle array, $\lambda_{RAs} \sim 601$ nm and we get $n_{eff} = 1.431$.

Considering the same slope of RAs and SLRs, we obtain the n_{eff} of 1L ($n_{eff} = 1.443$) to 4L ($n_{eff} = 1.481$) and a variation of n_{eff} per layer of 0.012. Such large change of effective refractive index

by just adding an atomic layer on top of the particle array highlights the strong interaction

between the field around the particle array and the high background refractive index ($n = 2.76$,

see Figure S4c) of WS$_2$. In addition, the linear response of n_{eff} in Figure 4b suggests that the

interacting field amplitude in 0L and 4L can be considered as a constant.

Table 1 Coupling parameters and evaluation of the strong coupling regimes.

	$k_{//}$ (μm^{-1})	Γ_{SLRs} (meV)	γ_A (meV)	Ω_R (meV)	$\Omega_R^2 > (\Gamma_{SLRs}^2 + \gamma_A^2)/2$	$\Omega_R > \Gamma_{SLRs}, \gamma_A$
1L[a]	3.5[I], 4.4[II]	54[I], 60[II]	28[I], 25[II]	47[I], 52[II]	yes	no
2L	3.7	55	59	58	yes	no
4L	4.5	61	62	78	yes	yes
16L	5.3	67	60	100	yes	yes

[a] Two different 1L samples (I and II) on the particle array were characterized.

We continue the analysis with a comparison of the coupling strength between the SLRs and

the excitons in WS$_2$ flakes of different thicknesses. We summarize the key coupling parameters

in Table 1, including the resonant in-plane wave-vector $k_{//}$, the corresponding Γ_{SLRs}, γ_A, Ω_R and

the evaluation of the strong coupling regime. Table 1 shows that the higher quality of 1L on

sample II (with a bare absorptance of 13% at $\omega_A = 2.023$ eV, Figure S5a) yields a slightly higher

coupling strength compared to 1L on sample I. From the Ω_R in table 1, we can clearly see that

the coupling strength is enhanced by increasing the number of layers from 1L to 16L. However,

Ω_R as a function of $\sqrt{N_L}$ (black dots in Figure 4c) in the case of ML is significantly lower than

the value expected from the formula of collective strong coupling $\Omega_R \propto \sqrt{N_L}$,[51] as noted by the

dashed line in Figure 4c. This reveals that the scalar multiplication of $\boldsymbol{E}$ and $\boldsymbol{\mu}$ as a function of

$\sqrt{N_L}$ must decrease.

In order to claim strong coupling, we have to consider both the anti-crossing and the

dynamics of the coupled system ruled by the competition between coherent Rabi-oscillations

and various decoherence processes of the coupled system. The weak criterion of strong coupling

is $\Omega_R{}^2 > (\gamma_A{}^2 + \Gamma_{SLRs}{}^2)/2$, namely, the splitting energy needs to be larger than the averaged

damping rate of the bare oscillators in order to guarantee observation of two new peaks.[34] A

stricter criterion is that the Rabi energy needs to overcome all the damping rates of the

individual oscillators, i.e, $\Omega_R > \gamma_A$, Γ_{SLRs}. We evaluate both criterions and summarize them in

the last two columns of Table 1. The coupling between the nanoparticle arrays with 1L to 16L

WS$_2$ can reach the strong coupling regime under the weak criterion. For satisfying the strong

criterion, we need to overcome the broad linewidth of SLRs for the case of 1L and enhance the

coupling strength further for 2L.

To fully understand the coupling efficiency of SLRs with the 1L and the ML, we have

simulated the anisotropic field enhancement distribution on a bare particle array and with a

flake on the array using the finite-element method (details in **Methods**). The same parameters

of the experimental geometry were used for the simulations, obtaining a similar bare SLR

angular dispersion to the experiments (Figure 5a). Note that the simulated dispersion of bare

SLRs is plotted herein as a function of in-plane wave vector distributed in PDMS instead of air

during the measurements. When the 1L WS$_2$ is placed on the particle array (Figure 5b), the

original bare SLR band displays a Rabi energy of 43 meV, a bit smaller than the experimental

value (52 meV). The electric field intensity enhancement factor of the SLRs compared to free

space at the energy of A excitons was calculated in terms of in-plane ($|E_{xy}|^2/|E_0|^2$) and out-of-

plane components ($|E_z|^2/|E_0|^2$), respectively. In these calculations, we consider the background

refractive index of WS_2. Due to the typical Fano-type resonance of SLRs, we scan the angle of

incidence around the SLR peaks to get the highest value of field intensity enhancement. The

field distribution in the planes xz and yz through the center of the nanorod, and in the plane xy

at a height $z = 3$ nm for 0L and $z = 8$ nm for 16L above the topmost surface of the particle array

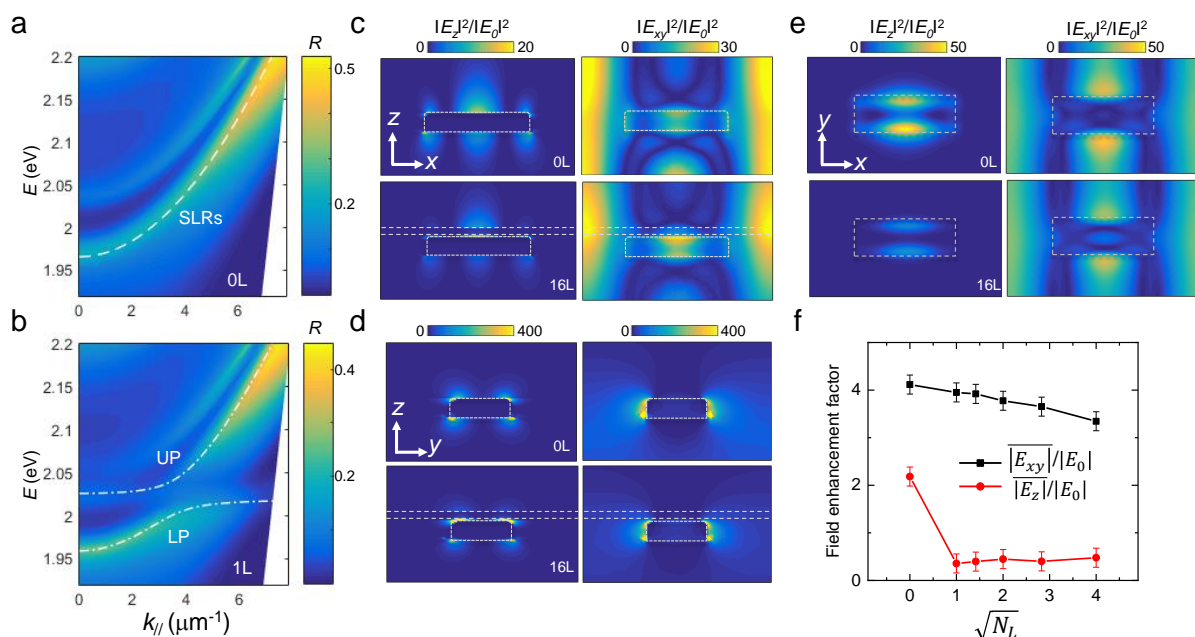are shown in Figures 5c, d, and e, respectively.

Figure 5. *Finite-element simulations of spectra and field distributions*. Angle-resolved reflection spectra simulation of the bare particle array (a), and of the 1L WS_2 on the array (b). The spectra are simulated for *p*-(TM) polarization and the angular dispersion of the 1L on the array is fitted with the coupled oscillator model. The dashed-white curve in (a) describes the dispersion of the SLRs of the bare particle array. The upper and lower dashed-dotted white curves in (b) represent the dispersion of the UP and LP band, respectively. Simulated out-of-plane ($|E_z|^2/|E_0|^2$, left column) and in-plane ($|E_{xy}|^2/|E_0|^2$, right column) field intensity enhancement at the energy of A excitons in the planes xz (c), yz (d), and xy (e) of a lattice unit cell. In (c) and (d), the field is analyzed by cutting through the center of the nanoparticle. The top and bottom row of the images in (c)-(e) corresponds to the result of 0L and 16L on the particle array, respectively. In (e), the field is calculated at a height of $z = 3$ nm above the array of the bare SLRs and $z = 8$ nm for 16L on top of the array. The dashed rectangular and horizontal lines in the field distribution images (c)-(e) represent the boundaries of the nanoparticles and WS_2 flake, respectively. (f) Field amplitude enhancement factor as a function of $\sqrt{N_L}$. The field is averaged over a lattice unit cell at the height corresponding to the center of the flake. The black squares and red circles represent the in-plane and out-of-plane field components, respectively. The error on the field enhancement factor stems from the variations observed when employing different meshing methods.

Due to the high permittivity contrast between WS_2 and its dielectric surrounding, the normal field ($|E_z|^2/|E_0|^2$ shown in the left column of Figures 5c and d) displays a strong discontinuity and is largely screened in the high refractive index WS_2 layer, as a consequence of the boundary condition of Maxwell equation (continuity of εE_z). In contrast, the profile of the in-plane ($|E_{xy}|^2/|E_0|^2$) field is only slightly modified by the existence of the WS_2 flake (right column of Figures 5c and d) except for a slightly weaker intensity. The in-plane electric field is not only confined to the particles but also extends into the surrounding dielectric medium. However, the out-of-plane component is mostly localized close to the particles. As shown in Figure 5f and Figure S10, both absolute amplitude enhancement factors, averaged over a lattice unit cell, decrease with WS_2 on top of the particle array and the in-plane field is ~ 8 times larger than the out-of-plane component. The different spatial overlap between in-plane and out-of-plane field components and the screened out-of-plane field in WS_2 suggest that the interaction of excitonic dipoles with the normal field can be disregarded. Therefore, we can calculate the ratio of the coupling efficiency of SLRs with ML and 1L based on the relationship, $\Omega_R \propto 2\sqrt{N_L}E \cdot \mu \approx 2\sqrt{N_L}|E_{xy}|\mu_{xy}$, with in-plane excitonic dipole μ_{xy} (Figure 1d) and field distribution in the flake $|E_{xy}|$ (Figure 5f). For simplicity in this calculation, we have used the averaged field amplitude, $\overline{|E_{xy}|}$, in a single lattice unit. We plot the estimated Rabi energy of ML as blue triangles in Figure 4c, finding a remarkable good agreement with the measurements. We also carried out the simulations of the angle-resolved dispersion of 2L, 4L, 10L and 16L WS_2 on the particle array (shown in Figure S11), considering only the in-plane transition dipoles of excitons in WS_2. The simulated value of Rabi-energy, plotted in Figure 4d, compares well with the experimental data. Both analyzed and simulated results confirm that the Rabi energy in our system stems mostly from in-plane coupling and saturates around 16L. Consequently, the periodic nanoparticle array can essentially strongly couple with both 1L and ML.

Using $\Omega_R = 2\sqrt{N}\boldsymbol{E}\cdot\boldsymbol{\mu}$, we can give an estimate of the number of coupled excitons, N, in WS_2 using the dipole moments of WS_2 and the vacuum field amplitude $E = \sqrt{\hbar\,\omega/(2\mathcal{E}\mathcal{E}_0 V)}$.[18,52] The mode volume (V) of delocalized SLRs can be defined by the in-plane coherent scattering length and the out-of-plane decay length of the field. We estimate the coherence length as ~ 1.7 µm from the group velocity of SLRs ($v_g \sim 0.08$ c) at the resonant wave vector obtained from the dispersion and dephasing lifetime ($\tau \sim 68$ fs) obtained from the resonance linewidth.[53] Hence, E supported by the particle array is estimated to $\sim 3.5 \times 10^5$ V/m and N is ~ 3000 for the case of 1L. This value of N is the of same order as reported by the coupling of 1L WS_2 with propagating surface plasmon polaritons on a metallic grating.[54]

In summary, we have demonstrated the strong coupling of direct transition excitons in monolayers and multilayers of WS_2 with collective plasmonic resonances in open plasmonic cavities formed by arrays of metallic nanoparticles at room temperature. The Rabi energy increases by increasing the number of layers. However, this increase does not scale with the square root of the number of layers. Only in-plane coupling contributes to the Rabi energy on the nanoparticle array due to the screened out-of-plane field distribution in WS_2. The decreased in-plane dipole moments of thicker WS_2 multilayers result in a smaller Rabi energy than the expected value from collective strong coupling. Understanding the mechanisms that increase and limit the coupling strength in 2D semiconductors and controlling this coupling is of utmost importance for the modification of the material properties by light-matter hybridization and the development of polaritonic devices. For instance, exciton-polaritonic states with ultrashort lifetimes in TMD multilayer systems could be used to suppress the inter-valley scattering and consequently enhance the degree of valley/spin polarization at room temperature. Polaritonic states could also be used to enhance the photoluminescence quantum yield of the direct transition excitons in multilayers. Furthermore, the collective and delocalized properties of polaritons and the investigated open cavities of nanoparticle arrays could be promising

platforms to enhance exciton transport,[28,29] and to achieve long-distance energy transfer in 2D

semiconductor devices.[30,31]

METHODS

Sample fabrication. The silver particle array was fabricated onto a fused silica substrate by

electron beam lithography and passivated with a 3 nm thick layer of Al_2O_3 deposited with

atomic layer deposition at ~ 100 °C. High-quality atomically thin WS_2 flakes were mechanically

exfoliated from a synthetic single crystal (hq graphene), and the thicknesses of the flake samples

were determined with white light microscope imaging, extinction, PL spectroscopy, and atomic

force microscopy (AFM). The WS_2 flakes were exfoliated onto an optically transparent and

flexible PDMS substrate. The flakes on the PDMS were aligned and softly deposited under a

microscope onto the silver particle array by surface adhesion. The thickness of the 16 layers of

WS_2 was measured with AFM to be 9.9 ± 0.4 nm (Figures S1 and S2).

Transmission, reflection and PL measurements. The transmittance spectra of the sample

were measured using an optical microscope under normal incidence. The samples were aligned

along the optical axis of the microscope and illuminated with quasi-collimated white light from

a halogen lamp. The light transmitted by the samples was collected using a microscope

objective lens (Nikon CFI S Plan Fluor ELWD 60x, NA = 0.7) and imaged by a spectrometer

(Princeton Instruments SpectraPro 300i) and an electron-multiplying charge-coupled device

camera (Princeton Instruments ProEM: 512). The extinction is recorded as 1-T, where T is the

transmittance of the sample. The reflection and PL spectra of all the samples were measured

using a microscope reflectometry setup equipped for optical Fourier analysis. The setup is

described in detail elsewhere.[15,22] A minimum sample size of 6.7 x 6.7 μm^2, selected by a 400

μm pinhole in the confocal plane, can be measured in the Fourier setup.

Angular dispersion of SLRs. The SLR dispersion curves extracted from the peaks of the

reflection spectra of the bare particle array were fitted with a two coupled oscillator model,

17

describing the interaction between the LSPRs of the individual particles and degenerate (0, ±1) RA respectively.[38] The RA dispersion follows the grating equation $\pm k_{//d} = k_{//i} + G$, where $k_{//d}$ = $(2\pi/\lambda)n_{eff} \cdot u_d$ and $k_{//i} = (2\pi/\lambda)\sin(\theta) \cdot u_i$ are the parallel-to-the-surface components of the diffracted and incident wave vectors, respectively, u_d and u_i are the unitary vectors along the diffracted and incident directions projected on the plane of the array, $G = (2\pi m/p_x, 2\pi n/p_y)$ is the reciprocal lattice vector with (m, n) defining the diffraction order and (p_x, p_y) the lattice constants of the array, θ is the angle between the wave vector of the incident beam and the direction normal to the plane of the array, and n_{eff} is the effective refractive index defining the phase velocity of the RAs.

Numerical simulations. The simulations were performed using the commercial finite-element method software COMSOL Multiphysics 5.2. We simulate only one unit cell of the periodic array by surrounding a single silver nanorod with Floquet periodic conditions. The nanorods were modeled as parallelepipeds where we replaced the sharp corners by sphere sections of radius 10 nm to avoid extreme hotspots and to approach the experimental conditions. A dispersionless model was used for the fused silica substrate, alumina spacer and PDMS superstrate. The optical constants of silver were obtained from Palik's handbook,[55] while the optical constants of WS_2 are obtained from the experimental results shown in Figures S4c and d. Considering the little difference between in-plane and out-of-plane dielectric constant of WS_2,[56] we used the uniform background refractive index ($n = 2.76$) for WS_2 crystal during the simulation. To avoid the problem of meshing layers smaller than the nanoscale, we simulate the interaction with the WS_2 monolayer with a surface conductivity, related to the permittivity as $\sigma = -i\epsilon_0\omega d[\varepsilon_{WS_2}(\omega) - 1]$,[57] with d the thickness of the WS_2 monolayer and ε_{WS_2} its permittivity.

ASSOCIATED CONTENT

Supporting Information

The description of sample I and II, refractive index and absorption spectra of WS_2, angle-resolved reflection spectra of the bare flake, coupled oscillator model fits to sample I and II, normal incidence spectra of the flake on array, and elctric field enhancement factor are attached in the supporting information (SI).

AUTHOR INFORMATION

Corresponding Author

*E-mail: s.wang@differ.nl

*E-mail: j.gomez.rivas@tue.nl

Notes

The authors declare no competing financial interest.

ACKNOWLEDGEMENTS

REFERENCES

(1) Mak, K. F.; Lee, C.; Hone, J.; Shan, J.; Heinz, T. F. Atomically Thin MoS_2: A New Direct-Gap Semiconductor. *Phys. Rev. Lett.* **2010**, *105*, 136805.

(2) Splendiani, A.; Sun, L.; Zhang, Y.; Li, T.; Kim, J.; Chim, C. Y.; Galli, G.; Wang, F. Emerging Photoluminescence in Monolayer MoS_2. *Nano Lett.* **2010**, *10*, 1271–1275.

(3) Mak, K. F.; Shan, J. Photonics and Optoelectronics of 2D Semiconductor Transition Metal Dichalcogenides. *Nat. Photonics* **2016**, *10*, 216–226.

(4) Zhao, C.; Gan, X.; Yuan, Q.; Hu, S.; Fang, L.; Zhao, J. High-Performance Volatile Organic Compounds Microsensor Based on Few-Layer MoS_2-Coated Photonic Crystal Cavity. *Adv. Opt. Mater.* **2018**, *6*, 1700882.

(5) Fatih Cihan, A.; Curto, A. G.; Raza, S.; Kik, P. G.; Brongersma, M. L. Silicon Mie Resonators for Highly Directional Light Emission from Monolayer MoS_2. *Nat.*

Photonics **2018**, *12*, 284–290.

(6)   Shi, J.; Liang, W.-Y.; Raja, S. S.; Sang, Y.; Zhang, X.-Q.; Chen, C.-A.; Wang, Y.; Yang, X.; Lee, Y.-H.; Ahn, H.; et al. Plasmonic Enhancement and Manipulation of Optical Nonlinearity in Monolayer Tungsten Disulfide. *Laser Photon. Rev.* **2018**, *12*, 1800188.

(7)   Wang, G.; Chernikov, A.; Glazov, M. M.; Heinz, T. F.; Marie, X.; Amand, T.; Urbaszek, B. Excitons in Atomically Thin Transition Metal Dichalcogenides. *Rev. Mod. Phys.* **2017**, *90*, 21001.

(8)   Ramasubramaniam, A. Large Excitonic Effects in Monolayers of Molybdenum and Tungsten Dichalcogenides. *Phys. Rev. B* **2012**, *86*, 115409.

(9)   Qiu, D. Y.; Da Jornada, F. H.; Louie, S. G. Optical Spectrum of MoS_2: Many-Body Effects and Diversity of Exciton States. *Phys. Rev. Lett.* **2013**, *111*, 176801.

(10)   Jones, A. M.; Yu, H.; Ghimire, N. J.; Wu, S.; Aivazian, G.; Ross, J. S.; Zhao, B.; Yan, J.; Mandrus, D. G.; Xiao, D.; et al. Optical Generation of Excitonic Valley Coherence in Monolayer WSe_2. *Nat. Nanotechnol.* **2013**, *8*, 634–638.

(11)   Onga, M.; Zhang, Y.; Ideue, T.; Iwasa, Y. Exciton Hall Effect in Monolayer MoS_2. *Nat. Mater.* **2017**, *16*, 1193–1197.

(12)   Liu, X.; Galfsky, T.; Sun, Z.; Xia, F.; Lin, E. C.; Lee, Y. H.; Kéna-Cohen, S.; Menon, V. M. Strong Light-Matter Coupling in Two-Dimensional Atomic Crystals. *Nat. Photonics* **2014**, *9*, 30–34.

(13)   Dufferwiel, S.; Schwarz, S.; Withers, F.; Trichet, A. A. P.; Li, F.; Sich, M.; Del Pozo-Zamudio, O.; Clark, C.; Nalitov, A.; Solnyshkov, D. D.; et al. Exciton-Polaritons in van Der Waals Heterostructures Embedded in Tunable Microcavities. *Nat. Commun.* **2015**, *6*, 1–7.

(14)   Liu, W.; Lee, B.; Naylor, C. H.; Ee, H. S.; Park, J.; Johnson, A. T. C.; Agarwal, R. Strong Exciton-Plasmon Coupling in MoS_2 Coupled with Plasmonic Lattice. *Nano Lett.* **2016**, *16*, 1262–1269.

(15)   Wang, S.; Li, S.; Chervy, T.; Shalabney, A.; Azzini, S.; Orgiu, E.; Hutchison, J. A.; Genet, C.; Samorì, P.; Ebbesen, T. W. Coherent Coupling of WS_2 Monolayers with Metallic Photonic Nanostructures at Room Temperature. *Nano Lett.* **2016**, *16*, 4368–4374.

(16)   Kleemann, M. E.; Chikkaraddy, R.; Alexeev, E. M.; Kos, D.; Carnegie, C.; Deacon, W.; De Pury, A. C.; Große, C.; De Nijs, B.; Mertens, J.; et al. Strong-Coupling of WSe_2 in Ultra-Compact Plasmonic Nanocavities at Room Temperature. *Nat. Commun.* **2017**, *8*, 1296.

(17)   Jaynes, E. T.; Cummings, F. W. Comparison of Quantum and Semiclassical Radiation Theories with Application to the Beam Maser. *Proc. IEEE* **1963**, *51*, 89–109.

(18)   Haroche, S.; Raimond, J. M. *Exploring the Quantum: Atoms, Cavities, and Photons*; 2006.

(19)   Tavis, M. Exact Solution for an N-Molecule-Radiation-Field Hamiltonian. *Phyical Rev.* **1968**, *170*, 379–384.

(20)   Flatten, L. C.; He, Z.; Coles, D. M.; Trichet, A. A. P.; Powell, A. W.; Taylor, R. A.; Warner, J. H.; Smith, J. M. Room-Temperature Exciton-Polaritons with Two-

Dimensional WS_2. *Sci. Rep.* **2016**, *6*, 33134.

(21) Zhang, L.; Gogna, R.; Burg, W.; Tutuc, E.; Deng, H. Photonic-Crystal Exciton-Polaritons in Monolayer Semiconductors. *Nat. Commun.* **2018**, *9*, 713.

(22) Chervy, T.; Azzini, S.; Lorchat, E.; Wang, S.; Gorodetski, Y.; Hutchison, J. A.; Berciaud, S.; Ebbesen, T. W.; Genet, C. Room Temperature Chiral Coupling of Valley Excitons with Spin- Momentum Locked Surface Plasmons. *ACS Photonics* **2018**, *5*, 1281–1287.

(23) Wen, J.; Wang, H.; Wang, W.; Deng, Z.; Zhuang, C.; Zhang, Y.; Liu, F.; She, J.; Chen, J.; Chen, H.; et al. Room temperature Strong Light-Matter Interaction with Active Control in Single Plasmonic Nanorod Coupled with Two-Dimensional Atomic Crystals. *Nano Lett.* **2017**, *17*, 4689–4697.

(24) Liu, W.; Wang, Y.; Naylor, C. H.; Lee, B.; Zheng, B.; Liu, G.; Johnson, A. T. C.; Pan, A.; Agarwal, R. Understanding the Different Exciton-Plasmon Coupling Regimes in Two-Dimensional Semiconductors Coupled with Plasmonic Lattices: A Combined Experimental and Unified Equation of Motion Approach. *ACS Photonics* **2018**, *5*, 192–204.

(25) Sukharev, M.; Pachter, R. Effects of Exciton-Plasmon Strong Coupling on Third Harmonic Generation by Two-Dimensional WS_2 at Periodic Plasmonic Interfaces. *J. Chem. Phys.* **2018**, *148*, 094701.

(26) Chakraborty, B.; Gu, J.; Sun, Z.; Khatoniar, M.; Bushati, R.; Boehmke, A. L.; Koots, R.; Menon, V. M. Control of Strong Light-Matter Interaction in Monolayer WS_2 Through Electric Field Gating. *Nano Lett.* **2018**, *18*, acs.nanolett.8b02932.

(27) Stührenberg, M.; Munkhbat, B.; Baranov, D. G.; Cuadra, J.; Yankovich, A. B.; Antosiewicz, T. J.; Olsson, E.; Shegai, T. Strong Light-Matter Coupling between Plasmons in Individual Gold Bipyramids and Excitons in Mono- and Multilayers of WSe_2. *Nano Lett.* **2018**, acs.nanolett.8b02652.

(28) Feist, J.; Garcia-Vidal, F. J. Extraordinary Exciton Conductance Induced by Strong Coupling. *Phys. Rev. Lett.* **2015**, *114*, 1–5.

(29) Rozenman, G. G.; Akulov, K.; Golombek, A.; Schwartz, T. Long-Range Transport of Organic Exciton-Polaritons Revealed by Ultrafast Microscopy. *ACS Photonics* **2018**, *5*, 105–110.

(30) Zhong, X.; Chervy, T.; Zhang, L.; Thomas, A.; George, J.; Genet, C.; Hutchison, J. A.; Ebbesen, T. W. Energy Transfer between Spatially Separated Entangled Molecules. *Angew. Chemie - Int. Ed.* **2017**, *56*, 9034–9038.

(31) Garcia-Vidal, F. J.; Feist, J. Long-Distance Operator for Energy Transfer. *Science*. 2017, pp 1357–1358.

(32) Hugall, J. T.; Singh, A.; van Hulst, N. F. Plasmonic Cavity Coupling. *ACS Photonics* **2018**, *5*, 43.

(33) Baranov, D. G.; Wersäll, M.; Cuadra, J.; Antosiewicz, T. J.; Shegai, T. Novel Nanostructures and Materials for Strong Light-Matter Interactions. *ACS Photonics* **2018**, *5*, 24–42.

(34) Törmä, P.; Barnes, W. L. Strong Coupling between Surface Plasmon Polaritons and Emitters: A Review. *Reports Prog. Phys.* **2015**, *78*, 013901.

21

(35)   Vecchi, G.; Giannini, V.; Gómez Rivas, J. Surface Modes in Plasmonic Crystals Induced by Diffractive Coupling of Nanoantennas. *Phys. Rev. B* **2009**, *80*, 201401.

(36)   Rodriguez, S. R. K.; Schaafsma, M. C.; Berrier, A.; Gómez Rivas, J. Collective Resonances in Plasmonic Crystals: Size Matters. *Phys. B* **2012**, *407*, 4081–4085.

(37)   Wang, W.; Ramezani, M.; Väkeväinen, A. I.; Törmä, P.; Gómez Rivas, J.; Odom, T. W. The Rich Photonic World of Plasmonic Nanoparticle Arrays. *Mater. Today* **2017**, 10.1016/j.mattod.2017.09.002.

(38)   Rodriguez, S. R. K.; Feist, J.; Verschuuren, M. A.; Garcia Vidal, F. J.; Gómez Rivas, J. Thermalization and Cooling of Plasmon-Exciton Polaritons: Towards Quantum Condensation. *Phys. Rev. Lett.* **2013**, *111*, 166802.

(39)   Ramezani, M.; Halpin, A.; Fernández-Domínguez, A. I.; Feist, J.; Rodriguez, S. R.-K.; Garcia-Vidal, F. J.; Gómez Rivas, J. Plasmon-Exciton-Polariton Lasing. *Optica* **2017**, *4*, 31.

(40)   Abass, A.; Rodriguez, S. R. K.; Gómez Rivas, J.; Maes, B. Tailoring Dispersion and Eigenfield Profiles of Plasmonic Surface Lattice Resonances. *ACS Photonics* **2014**, *1*, 61–68.

(41)   Ramezani, M.; Halpin, A.; Feist, J.; Van Hoof, N.; Fernández-Domínguez, A. I.; Garcia-Vidal, F. J.; Gómez Rivas, J. Dispersion Anisotropy of Plasmon-Exciton-Polaritons in Lattices of Metallic Nanoparticles. *ACS Photonics* **2018**, *5*, 233–239.

(42)   Wang, S.; Le-van, Q.; Peyronel, T.; Ramezani, M.; Hoof, N. Van; Tiecke, T. G.; Go, J. Plasmonic Nanoantenna Arrays as Efficient Etendue Reducers for Optical Detection. *ACS Photonics* **2018**, *5*, 2478–2485.

(43)   Zakharko, Y.; Rother, M.; Graf, A.; Hähnlein, B.; Brohmann, M.; Pezoldt, J.; Zaumseil, J. Radiative Pumping and Propagation of Plexcitons in Diffractive Plasmonic Crystals. *Nano Lett.* **2018**, *18*, 4927–4933.

(44)   Li, Y.; Chernikov, A.; Zhang, X.; Rigosi, A.; Hill, H. M.; Van Der Zande, A. M.; Chenet, D. A.; Shih, E. M.; Hone, J.; Heinz, T. F. Measurement of the Optical Dielectric Function of Monolayer Transition-Metal Dichalcogenides: MoS_2, $MoSe_2$, WS_2, and WSe_2. *Phys. Rev. B* **2014**, *90*, 205422.

(45)   Ye, Z.; Cao, T.; O'Brien, K.; Zhu, H.; Yin, X.; Wang, Y.; Louie, S. G.; Zhang, X. Probing Excitonic Dark States in Single-Layer Tungsten Disulphide. *Nature* **2014**, *513*, 214–218.

(46)   Zhao, W.; Ribeiro, R. M.; Toh, M.; Carvalho, A.; Kloc, C.; Castro Neto, A. H.; Eda, G. Origin of Indirect Optical Transitions in Few-Layer MoS_2, WS_2, and WSe_2. *Nano Lett.* **2013**, *13*, 5627–5634.

(47)   George, J.; Wang, S.; Chervy, T.; Canaguier-Durand, A.; Schaeffer, G.; Lehn, J.-M.; Hutchison, J. A.; Genet, C.; Ebbesen, T. W. Ultra-Strong Coupling of Molecular Materials: Spectroscopy and Dynamics. *Faraday Discuss.* **2015**, *178*, 281–294.

(48)   Fano, U. Effects of Configuration Interaction on Intensities and Phase Shifts. *Phys. Rev.* **1961**, *124*, 1866–1878.

(49)   Shi, L.; Hakala, T. K.; Rekola, H. T.; Martikainen, J. P.; Moerland, R. J.; Törmä, P. Spatial Coherence Properties of Organic Molecules Coupled to Plasmonic Surface Lattice Resonances in the Weak and Strong Coupling Regimes. *Phys. Rev. Lett.* **2014**,

112, 153002.

(50) Hopfield, J. J. Theory of the Contribution of Excitons to the Complex Dielectric Constant of Crystals. *Phys. Rev.* **1958**, *112*, 1555–1567.

(51) Salomon, A.; Wang, S.; Hutchison, J. A.; Genet, C.; Ebbesen, T. W. Strong Light-Molecule Coupling on Plasmonic Arrays of Different Symmetry. *ChemPhysChem* **2013**, *14*, 1882–1886.

(52) Wang, S.; Chervy, T.; George, J.; Hutchison, J. A.; Genet, C.; Ebbesen, T. W. Quantum Yield of Polariton Emission from Hybrid Light-Matter States. *J. Phys. Chem. Lett.* **2014**, *5*, 1433–1439.

(53) Vasa, P.; Wang, W.; Pomraenke, R.; Lammers, M.; Maiuri, M.; Manzoni, C.; Cerullo, G.; Lienau, C. Real-Time Observation of Ultrafast Rabi Oscillations between Excitons and Plasmons in Metal Nanostructures with J-Aggregates. *Nat. Photonics* **2013**, *7*, 128–132.

(54) Zhang, S.; Zhang, H.; Xu, T.; Wang, W.; Zhu, Y.; Li, D.; Zhang, Z.; Yi, J.; Wang, W. Coherent and Incoherent Damping Pathways Mediated by Strong Coupling of Two-Dimensional Atomic Crystals with Metallic Nanogrooves. *Phys. Rev. B* **2018**, *97*, 235401.

(55) Palik, E. D. *Handbook of Optical Constants of Solids, Academic Press: Orlando*; 1985.

(56) Meckbach, L.; Stroucken, T.; Koch, S. W. Influence of the Effective Layer Thickness on the Ground-State and Excitonic Properties of Transition-Metal Dichalcogenide Systems. *Phys. Rev. B* **2018**, *97*, 035425.

(57) Maier, S. A. *Plasmonics Fundamentals and Applications. Springer Science*; 2007.